Electrical and chemical properties of vacancy-ordered lead free layered double perovskite nanoparticles

SCHOLARONE™
Manuscripts

Electrical and chemical properties of vacancy-ordered lead free layered double perovskite nanoparticles

Amal Sawahreh[1], Tal Binyamin[1], Jie Jiang[2], Oded Millo[3], Oren Goldberg[3], Doron Azulay[3], Ruth Pachter[2], Lioz Etgar[1, *]

[1] Institute of Chemistry, Casali Center for Applied Chemistry and the Center for Nanoscience and Nanotechnology, The Hebrew University of Jerusalem, Jerusalem 91904, Israel.

[2] Air Force Research Laboratory, Materials and Manufacturing Directorate, Wright-Patterson Air Force Base, Ohio 45433, U.S.A.

[3] Racah Institute of Physics, The Hebrew University of Jerusalem and the Center for Nanoscience and Nanotechnology, Jerusalem 91904, Israel.

* lioz.etgar@mail.huji.ac.il

Abstract

In this work we synthesized vacancy-ordered lead-free layered double perovskite (LDP) nanoparticles. This structure consists of two layers of trivalent metal halide octahedra $[B(III)X_6]^{3-}$ separated by a layer of divalent metal $[B(II)X_6]^{4-}$ (B is a divalent or trivalent metal). The chemical formula of this structure is based on $A_4B(II)B(III)_2X_{12}$ where A is Cs, B (III) is Bi, X is Cl and B(II) is a different ratio between Mn^{+2} and Cd^{+2}. Well-defined colloidal nanoplates of $Cs_4Cd_xMn_{1-x}Bi_2Cl_{12}$ were successfully synthesized. These nanoplates show photoluminescence (PL) in the orange to red region that can be tuned by changing the Cd/Mn ratio. High resolution scanning transmission electron microscopy (HR-STEM) and atomic resolution elemental analysis were performed on these lead free LDP nanoplates revealing two different particle compositions that can be controlled by the Cd/Mn ratio. Ultraviolet Photoelectron Spectroscopy (UPS) and scanning tunneling spectroscopy (STS) reveal the band gap structure of these LDP nanoplates. Density functional theory (DFT) calculations show the existence of $[MnCl_6]^{4-}$ in-gap states. While the absorption occurs from the valence band maximum (VBM) to the conduction band

minimum (CBM), the emission may occur from the CBM to an in-gap band maximum (IGM), which could explain the PL in the orange to red region of these nanoplates. This work provides a detailed picture of the chemical and electronic properties of LDP nanoparticles.

Introduction

Lead halide perovskite nanoparticles (NPs) bearing the formula ABX_3, (where A and X are organic/inorganic monovalent cation and halide anion, respectively), are attractive materials due to their remarkable optical and electrical properties, such as high luminescence efficiency, tunable band gap throughout the visible spectrum and low-cost synthesis.[1,2,3] These excellent properties have driven to use of perovskite NPs in light emitting diodes (LEDs).[4,5] However, the existence of the toxic lead and the instability of the lead halide perovskite limit their commercialization.[6,7] In order to overcome the toxicity and the stability issues, it is inevitable to explore lead-free perovskites. Although many lead-free perovskite structures were reported, it is important to note that some lead-free perovskites contain other toxic elements,[8,9,10] however they demonstrate interesting and applicable optical properties which are essential to explore. One of the candidates to replace the lead is the trivalent metal B(III) based perovskites with the general formula $A_3B(III)_2X_9$, that creates a two-dimensional layered structure. This structure shows an improvement in stability and weakening in the optical properties because of its indirect bandgap nature.[11,12,13] Another option is to replace two of the Pb cations with one monovalent cation (B(I)) and one trivalent cation (B(III)) to form the so called double perovskite structure with the general formula $A_2B(I)B(III)_2X_6$.[14,15] However, this structure has an indirect bandgap and therefore isn't favorable to be used in photovoltaic (PV) applications.[16,17] To-date, none of the above lead-free perovskites NPs demonstrate the superior optical properties similar to the lead halide perovskite NPs.[18,19]

For instance, layered $Cs_3Bi_2X_9$ NPs show the highest PLQY of 19.4% in the case of X=Br, and 26.4% in the case of X=Cl. In addition double perovskite NPs based on $Cs_2AgIn_{0.9}Bi_{0.1}Cl_6$ demonstrate PLQY of 36.6%.[5,20] Recently, a new unique structure of lead-free perovskite has attracted attention, having the chemical formula of $A_4B(II)B(III)_2X_{12}$,[1,7,21] where divalent and trivalent metals replace the Pb. This unique

perovskite structure was named vacancy-ordered layered double perovskite (LDP). The vacancy-ordered perovskite is related to the structure in which one of three B-sites cations is not occupied and replaced by a vacancy.[10,22,23] This structure consists of two layers of trivalent metal halide octahedra $[B(III)X_6]^{3-}$ separated by a layer of divalent metal octahedra $[B(II)X_6]^{4-}$. These three layers of metal halide octahedra are surrounded by vacancy layers from both sides, thus constituting a two-dimensional layered structure.[24] To date, there are only a few reports on LDP with different compositions, in which the main focus is related to theoretical predictions of the band structure.[21-22,24-25]

In this work we synthesized lead-free LDP NPs with the formula $A_4B(II)B(III)_2X_{12}$, where A is Cs, B (III) is Bi, X is Cl and B(II) is a different ratio between Mn^{2+} and Cd^{2+}. We successfully synthesized well-defined colloidal nanoplates of $Cs_4Cd_xMn_{1-x}Bi_2Cl_{12}$ using trimethylsilyl chloride (TMSCl) as the halide precursor. These nanoplates show photoluminescence (PL) between orange to red region, which can be tuned by changing the Cd/Mn ratio. This PL region, 600-650 nm, is surprisingly very much redshifted with respect to the absorption edge, positioned at ~350 nm. We performed atomic resolution elemental analysis of these lead-free LDP nanoplates. Two different compositions of particles were found, which can be controlled by the Cd/Mn ratio. Using ultraviolet photoelectron spectroscopy (UPS) and scanning tunneling spectroscopy (STS) measurements we successfully draw the band diagram of these nanoplates, revealing direct band gap for these LDP nanoplates. Moreover, theoretical calculations suggest a supposition on the origin of the emission peak at 600-650 nm observed in these nanoplates.

Results and discussion
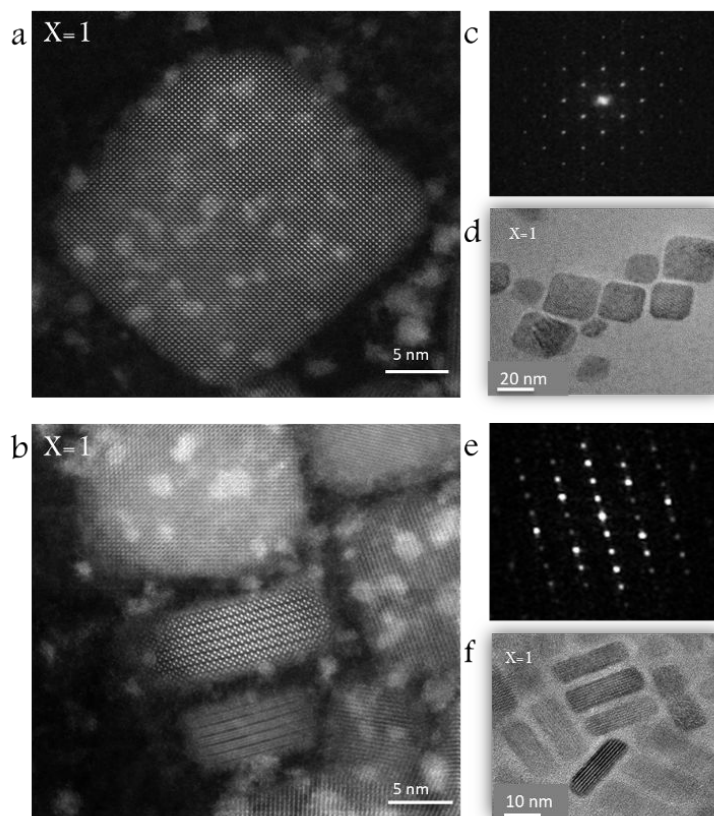
Figure 1: (a) HR-STEM image of single $Cs_4CdBi_2X_{12}$ (x=1) NP in zone axis: [1 0 1] and (c) the corresponding FFT; (b) HR-TEM image at low magnification of the NPs and (d) HR-STEM image of the NPs at different orientations- zone axis: [1 -1 0]; (e) The corresponding FFT; (f) HR-TEM image of the NPs in the same orientation as presented in figure 1b.

Lead-free LDP nanoplates were synthesized using a hot injection method, involving preparation of a solution containing Cs, Bi, and specific ratios of Cd/Mn cations, as described in detail in the experimental section and table S1 in the supporting information. During the synthesis all elements are present in the reaction flask, followed by the injection of TMSCl. Scanning transmission electron microscopy energy dispersive X-ray spectroscopy (STEM-EDS) was applied in order to preform elemental analysis at the atomic scale for these nanostructures.

Figure 1 presents structural analysis of pure $Cs_4CdBi_2Cl_{12}$ (x=1) NPs without Mn, where Figure 1a depicts an atomic resolution scanning transmission electron microscopy (STEM) image of a single particle. The electron diffraction pattern of this single particle appears in Figure 1b, where its fast Fourier transform (FFT) shows d-spacing values corresponding to

miller indices belonging to $Cs_4CdBi_2Cl_{12}$ structure in the zone axis [1 0 1]. Figure 1d presents another orientation of these particles, with their corresponding FFT (figure 1e), which reveals d-spacing and miller indices belongs to $Cs_4CdBi_2Cl_{12}$, but in a different zone axis [1 -1 0]. Additional zone axis [-1 -1 3] can be found in figure S7 for $Cs_4CdBi_2Cl_{12}$ NPs and the corresponding miller indexes. Based on the average edge length of the cubic particles in zone axis [1 0 1], and the edge length of the particles in zone axis [1 -1 0], we can conclude that the synthesized particles have a morphology of nanoplates, with lateral dimensions of 17.5 ± 1.3 nm and thickness of 7.7 ± 0.8 nm. (Size distribution histogram can be seen in figure S1 in the supporting information)
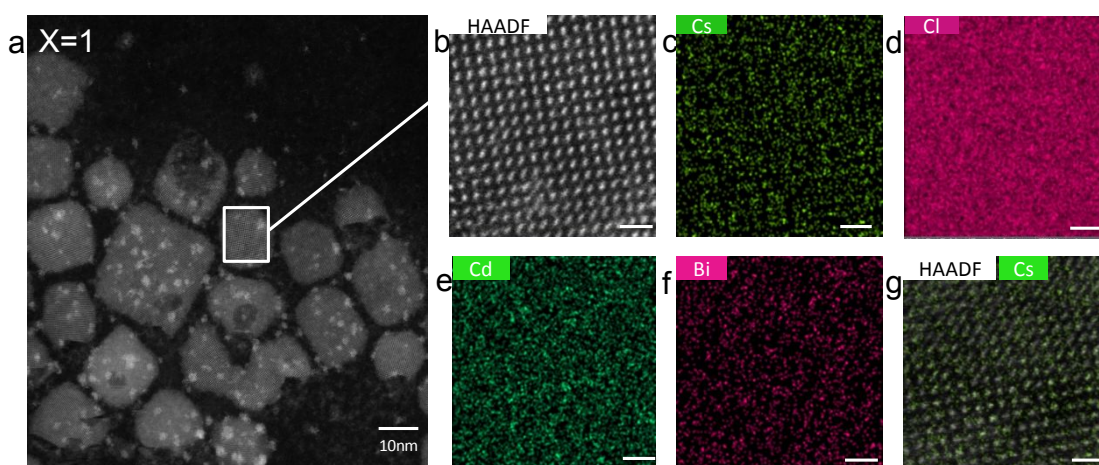
Figure 2: (a) High magnification STEM image of $Cs_4CdBi_2X_{12}$ (x=1) nanoplates; (b) HAADF STEM image of single particle with atomic resolution; (c), (d), (e), (f), (g) EDS maps of Cs, Cl, Cd, Bi; (g) overlapping between HAADF and Cs elemental map. The scale Bar is 1 nm.

High resolution STEM image of $Cs_4CdBi_2Cl_{12}$ nanoplates can be seen in figure 2a, corresponding to x=1, which shows the cubic shape of these nanoplates. EDS elemental mapping has been done on a single particle. Figure 2b presents the high-angle annular dark-field (HAADF) in atomic resolution of a single $Cs_4CdBi_2Cl_{12}$ particle. All the elements Cs, Cl, Cd, and Bi are observed in the analysis (Figure 2c-f, respectively), and distributed uniformly inside the particle.
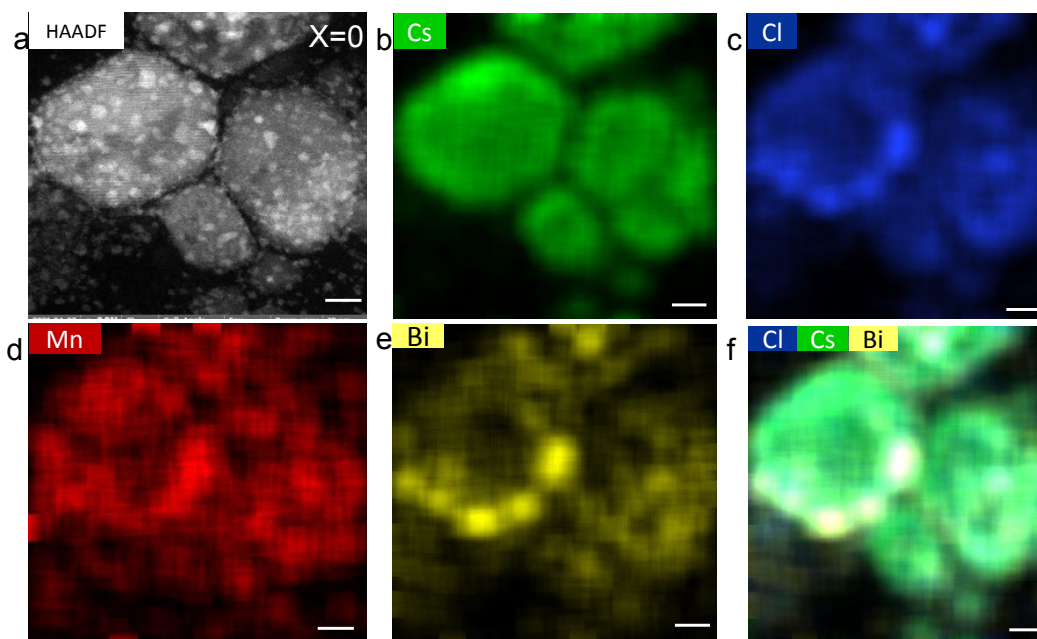
Figure 3: (a) HAADF-STEM of $Cs_4MnBi_2X_{12}$ (x=0) NPs. (b),(c),(d),(e),(f) EDS elemental maps of Cs, Cl, Mn, Bi. Scale bars: 10 nm.

Following the synthesis of x=1 which contains only Cd, also x=0 NPs, containing only Mn were synthesized. In contrast to the case of only Cd, the $Cs_4MnBi_2Cl_{12}$ NPs (x=0) shows a different morphology (hexagonal shape), as can be seen in the HAADF image in **Error! Reference source not found.** figure 3a. STEM-EDS elemental analysis of these particles portrays the different elements distributed in these particles (figures 3b-f), where the Mn is clearly observed inside the particles (see figure 3d).
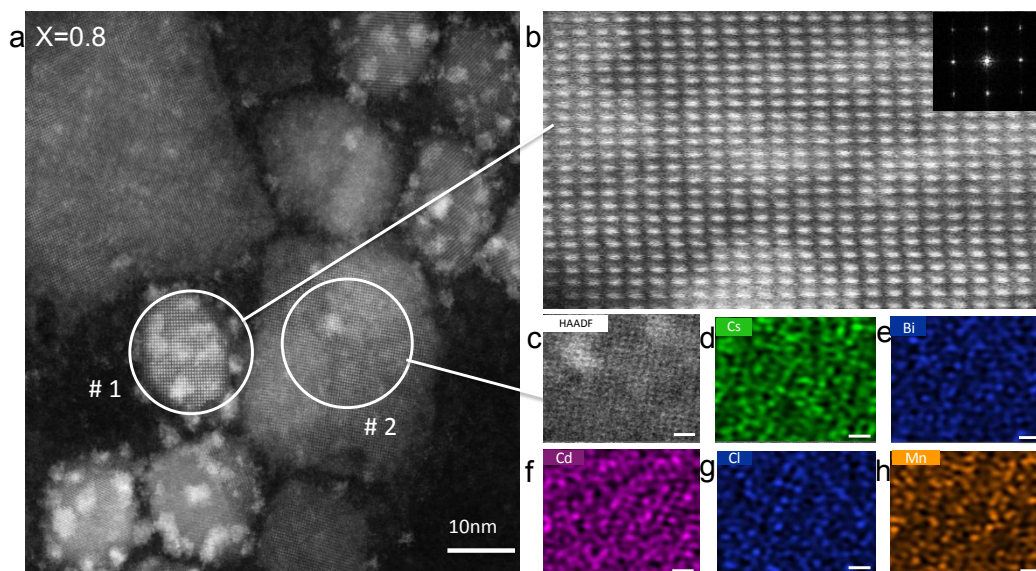
Figure 4: (a) STEM image of x=0.8 NPs; area # 1 represents a secondary product of the synthesis (Cs_3BiC_{l6} NP); area # 2 represents the desired product (LDP nanoplates); (b) Image lattice of Cs_3BiC_{l6} NP in zone axis of [1 0 1], inset- FFT of the NP; (c) HAADF STEM image of LDP nameplates, (d),(e),(f),(g),(h) STEM-EDS elemental maps for Cs, Cl, Cd, Bi, Mn. Scale bars: 1 nm.

Different ratios of Cd to Mn have been studied, for which a series of $Cs_4Cd_xMn_{1-x}Bi_2Cl_{12}$ NPs (with x=0.8, x=0.7, x=0.5) were synthesized. Figure 4 shows the HRTEM image of the x=0.8 perovskite. Two different types of NPs can be recognized in figure 4a, one corresponding to a secondary phase of the synthesis, Cs_3BiC_{l6}, (area #1) and the other to the desired X=0.8 nanoplate (area #2). Figures 4c-h show the EDS elemental mapping of area #2 which corresponds to $Cs_4Cd_{0.8}Mn_{0.2}Bi_2Cl_{12}$ nanoplates as was observed in x=1. The addition of 20% Mn didn't change the lead-free LDP crystal structure; moreover from the EDS mapping it can be observed that the Mn is present in these nanoplates (figure 4h). The secondary NPs population in the x=0.8 sample was analyzed in area #1 using HRTEM and FFT (see the inset of figure 4b). The analysis of the FFT pattern of this single particle provides d-spacing values and miller indices which match Cs_3BiC_{l6} crystal structure. The observed d-spacing of 0.362 nm matches the (1 1 3) crystallographic plane whereas the 0.255 nm d-spacing matches (-1 3 2) crystallographic plane (see table S2 and figure S2). To further support the observation of two phases X-ray diffraction (XRD) measurements were performed see figure S6. The XRD patterns of Cs_3BiCl_6 and of $Cs_4Cd_xMn_{1-x}Bi_2Cl_{12}$ are similar which makes it complicate to distinguish between their signals. However, small

differences can be observed clearly in the spectra as broad and asymmetric peaks which composed of two overlapping peaks, related to Cs_3BiCl_6 and $Cs_4Cd_xMn_{1-x}Bi_2Cl_{12}$. Such asymmetric peaks (hybridization of the two peaks) can be seen at 2Φ of 23° and 41°, where the shoulder at the large angles corresponds to $Cs_4Cd_xMn_{1-x}Bi_2Cl_{12}$. Due to the differences in the lattice parameters, a small shift in the XRD peaks of x=1 and x=0 also exists.[24] The XRD peaks in the case of full Mn^{2+} composition (x=0) are shifted slightly towards higher angles. In the case of mix Cd/Mn compositions the peaks of both NPs can be observed; in contrast to the case of pure Mn or Cd phases, where the peaks are sharper and more defined. When using Cs^+, Bi^{3+} and halide anions at different stoichiometric ratios and different amounts of capping ligands, several crystalline materials can be observed, where one product can be Cs_3BiCl_6, that consists of $[BiCl_6]^{3-}$ octahedra. Our synthesis was carried out at 150^0 C, with a ratio of 2 between Cs^+ to Bi^{3+} and large amount of Oleylamine, which according to previous reports[11] is considered as suitable conditions for the formation of Cs_3BiCl_6 NPs in addition to the main $Cs_4Cd_xMn_{1-x}Bi_2Cl_{12}$ nanoplates.
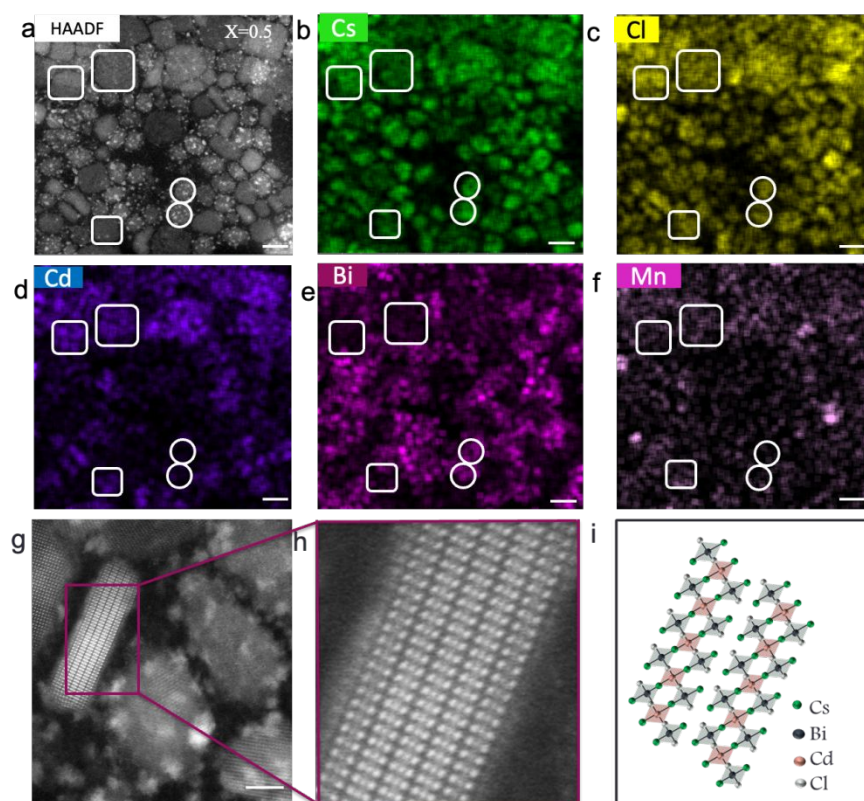
Figure 5 (a) High resolution STEM image of $Cs_4Cd_{0.5}Mn_{0.5}Bi_2Cl_{12}$ (x=0.5), (b),(c),(d),(e),(f) STEM-EDS elemental maps for Cs, Cl, Cd, Bi, Mn; The squares present the presence of the desired

nanoplates, where the circles show the Cs_3BiCl_6 NPs. Scale bars: 20 nm, (g) high resolution STEM image of nanoplates $Cs_4Cd_{0.5}Mn_{0.5}Bi_2Cl_{12}$(x=0.5). Scale bars: 5 nm; (h) enlargement of the area showing three lines of heavy metal atoms: Bi, Cd, Bi; (i) Schematic illustration of the layered structure.

The case of x=0.5 NPs is presented in figure 5a, where also two different types of particles are present in the solution. Figure 5b, c and e, show that Cs, Cl and Bi are observed in the two types of NPs, whereas Cd and Mn appear only in a particular population of NPs. Figure 5d and f depict the presence of Cd and Mn atoms only in the case of the cubic nanoplates (surrounded by square), while Cs_3BiCl_6 NPs (surrounded by circles) didn't show the presence of Cd and Mn.

The image lattice of single nanoplate (in the case of x=0.5), at zone axis [1 -1 0] can be observed in figure 5g and 5h. Three lines of heavy metals appear in the image, which corresponds to the vacancy-ordered layered double perovskite crystal structure as demonstrated schematically in figure 5i. The case of x=0.7 can be observed in figure S3 in the supporting information.
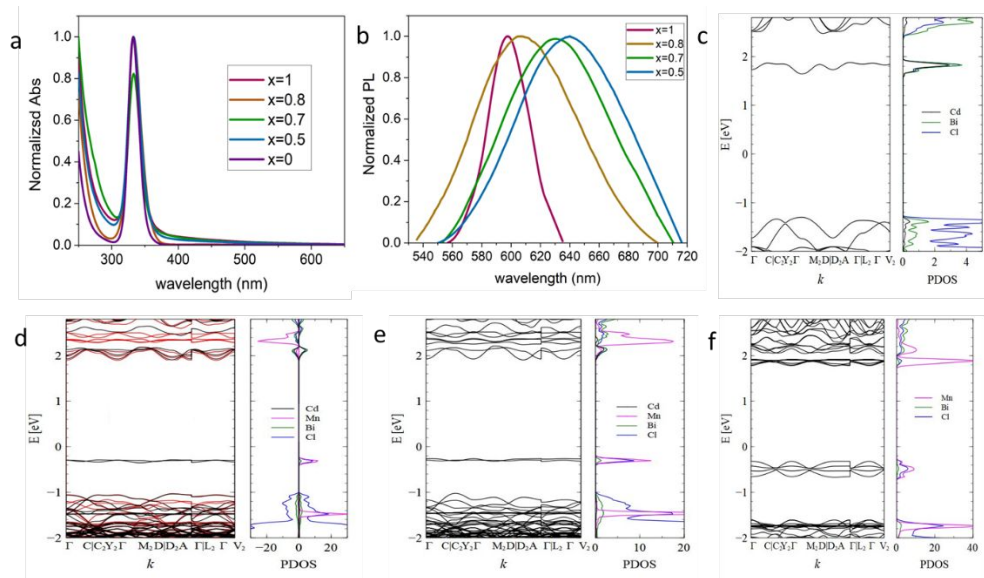
Figure 6:(a) Normalized absorbance spectra of x=1, 0.8, 0.7, 0.5, 0; (b) Normalized PL spectra for different Cd/Mn ratios; (c-g) Band structures and projected density of states (PDOS) for $Cs_4Cd_xMn_{1-x}Bi_2Cl_{12}$ with (c) x=1; (d) x=0.75; (e) x=0.50; (f) x=0.

The optical properties of LDPs were investigated and interpreted for nanoplates with different Cd/Mn ratios. Figure 6a presents the absorbance spectra of these nanoplates at different Cd/Mn ratios. The absorbance edges are identical for all cases and suggest a direct band gap for these nanoplates.[25] On the other hand, two interesting observations can be seen in the corresponding photoluminescence (PL) spectra. First, the PL peak wavelength are in the range of 590-650 nm, thus showing a large stokes shift from the absorbance edge (around ca. 320 nm). Second, the PL is redshifted as a function of the Cd/Mn ratio by an amount that increases with the Mn content.

In order to understand this unique optical behavior and to gain qualitative insight into the electronic and optical properties of LDPs when varying x (x=1, 0.75, 0.5 and 0), density functional theory (DFT) calculations were performed. The calculated electronic structure of $Cs_4Cd_xMn_{1-x}Bi_2Cl_{12}$ illustrate the emergence of in-gap states, except for pristine $Cs_4CdBi_2Cl_{12}$ (figure6 c), which can be attributed primarily to the $[MnCl_6]^{4-}$ moieties. These states have weak dispersions for x=0.75 and x=0.5 (figure 6d and e respectively), but become stronger for x=0 (figure 6f). The increase of the band dispersion with Mn percentage increase (x decrease) is suggested to be due to the reduced Mn-Mn distances and thus enhanced Mn-Mn interactions. We note that all atoms (except for Cs) contribute to the conduction band minimum (CBM) for $Cs_4Cd_xMn_{1-x}Bi_2Cl_{12}$, while the atomic orbital contributions to the valence band maximum (VBM) depend on the value of x. For $Cs_4CdBi_2Cl_{12}$ (X=1), the VBM is contributed by Cd, Bi and Cl, while for $Cs_4MnBi_2Cl_{12}$ (x=0) it is by Mn, Bi and Cl. In the case of $Cs_4Cd_xMn_{1-x}Bi_2Cl_{12}$ with 0<x<1, it is contributed by Bi and Cl only. We suggest rationalizing the emission process in comparison with the experimental results (shown in figure 6b) by the emergent in-gap states, as based on our electronic structure calculations. In the case of $Cs_4CdBi_2Cl_{12}$, for which no in-gap states occur, it is possible that electrons and holes funnel to external $[CdCl_6]^{4-}$ clusters, as proposed for Cd-doped $CsPbCl_3$.[26] On the other hand, in $Cs_4Cd_xMn_{1-x}Bi_2Cl_{12}$, $[MnCl_6]^{4-}$ in-gap states exist, and while the absorption occurs from the VBM and CBM, the emission may occur from the CBM and in-gap states maximum (IGM). When the Cd component is smaller than x=1 in $Cs_4Cd_xMn_{1-x}Bi_2Cl_{12}$, after aligning the top of the in-gap bands, we note that the CBM decreases in energy with a decrease in *x*, where the decrease in the Mn-Mn distances reduces the energy gap between the IGM and CBM. Since the energy gap

qualitatively corresponds to the emission energy, we expect the emission energy to redshift with increased Mn concentration; consistent with the trend of the PL spectra.
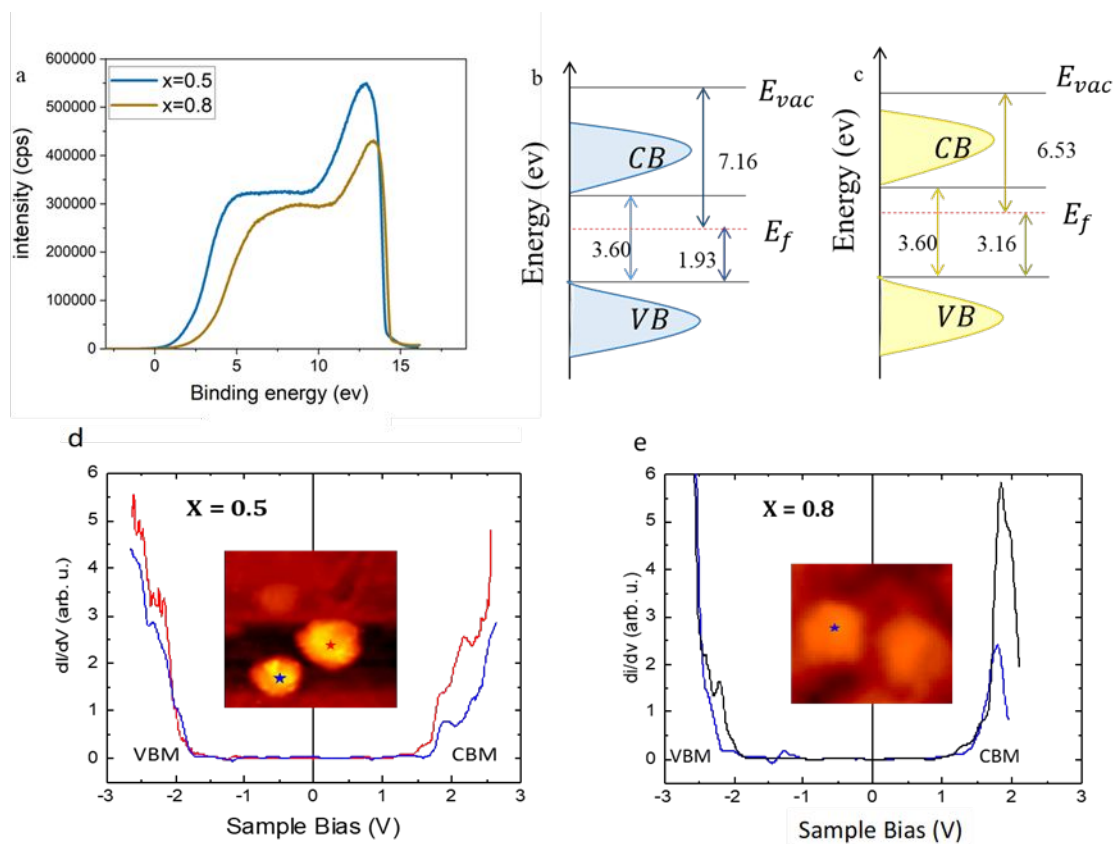
Figure 7: (a) Ultraviolet Photoelectron Spectroscopy (UPS) spectra of x=0.5 and x=0.8 NPs; (b-c) schematic energy level diagram of x=0.5 and x=0.8, respectively, based on the UPS and absorbance data. E_{vac} represents the vacuum level, E_F - Fermi level, CB is the conduction band and VB is the valence band. (d-e) typical tunneling spectra measured using STM on single nanoplates of x=0.5 (d) and x=0.8 (e) The insets present topographic images, 25×25 nm² (d) and 20×20 nm² in size, where the nanoplates on which the spectra were acquired are marked by asterisks with the corresponding colors.

In order to have a more quantitative picture on the nanoplates band gaps, Ultraviolet Photoelectron Spectroscopy (UPS) and scanning tunneling microscopy and spectroscopy (STM-STS) measurement were performed. The UPS measurement allows to experimentally determine the orbital energies in the valence region, where the change in the Mn content may influence the position of the energy levels in these nanomaterials. As shown in figure 7a-c, the work function increases with the decrease in Cd/Mn ratio, the measured work functions are 6.53 eV for x=0.8 and 7.16 eV for x=0.5. These results were

determined using $E_{vac} - E_F = E_{ph} - E_0$, where the source of the photon is He I (21.2ev), and E_0 is the cut-off energy (see table S3 for the parameters extracted from the UPS). It can be seen that when increasing x (more Mn in the nanoplates), the Fermi level is getting closer to the CBM which suggests the nanoplate becomes more n-type semiconductor.

For the STM-STS measurement a solution of NPs immersed in chloroform was drop-cast on a gold substrate film and let dry. After identifying a single NP, the STM tip was positioned over it and tunneling spectra were acquired in a double barrier tunnel junction configuration.[13,27] Typical dI/dV-V tunneling spectra, which are proportional to the NPs density of states, are presented in Figures 7d and S4 for x=0.5 NPs and Figure 7e for x=0.8 NPs. All spectra exhibit a band gap of ~3.6 eV, as determined from the mid-energy between the actual onset of observable DOS and the first peak or shoulder in the spectrum, consistent with the absorption and UPS data, both showing tailing to lower energies. Moreover, and also in qualitative agreement with the UPS measurements, the STS data show that the x=0.8 NPs are more n-type compared to their x=0.5 counterparts; this is evident by the smaller separation between E_F (V=0) and the CBM in the former compared with the latter case. Tunneling spectra measured aside of the NPs, on the Au substrate, show no gap structure, confirming that the chloroform molecules (that may remain on the substrate after drop-casting) do not add any spectral features (see Figure S5). However, the tunneling did show any evidence for in-gap states, unlike some cases where in-gap states giving rise to red-shifted PL of Si nanocrystals were found.[28,29] It should be noted, however, that in the case of the Si NPs the PL signal was much larger compared to what we observed here, signifying a larger relative amount of in-gap states, and they were also located at the Si nanocrystals surface, two important factors that making them easier to detect. Moreover, the band gaps of the Si nanocrystals studied in references 29 and 30 ranged between 2.1 to 1.3 eV (depending on nanocrystal size), much smaller compared with that of the perovskite DPL nanoplates studied here, and the in-gap states were also located energetically much closer to the band-edges of the Si nanocrystal, factors that also largely facilitate their observation in the Si particles.

Conclusion

In this work we present the synthesis of lead-free LDP nanoplates with the chemical formula $Cs_4Cd_xMn_{1-x}Bi_2Cl_{12}$. We changed the Cd/Mn ratio and tracked the optical, structural and electronic properties. Using STEM-EDS we performed atomic resolution analysis of the chemical elements in these nanoplates. When varying the Cd/Mn ratio two types of NPs having different composition were observed. Moreover, the absorbance didn't change upon the Cd/Mn ratio, while the PL was redshifted when increasing the Mn concertation inside the nanoplates. DFT calculations predict that in-gap states emerge in the band gap due to $[CdCl_6]^{4-}$ clusters, which can explain the very large redshift in the PL with respect to the absorption edge. UPS and STS measurements show the electronic structure of these lead free LDP band gap. This work sheds light on unique vacancy-ordered lead free layered double perovskite nanoplates, paving the way for new directions in lead free perovskite NPs.

Acknowledgment

Experimental section

Chemicals: Cesium acetate ($CsCH_3COO$),>=99.99% , Sigma-Aldrich), Bismuth(III) acetate ($Bi(CH_3COO)_3$,>=99.99%, Sigma-Aldrich),Manganese(II) acetate ($Mn(CH_3COO)_2$), 98%, Sigma-Aldrich), Cadmium(II) acetate anhydrous ($Cd(CH_3COO)_2$) 99.995%,Sigma-Aldrich, oleic acid (OA, 90%, Sigma-Aldrich), oleylamine (OLAM, 70%, Sigma-Aldrich), 1-octadecene (ODE, 90%, Sigma-Aldrich), Chlorotrimethylsilane (TMCS, purified by redistillation >=99%, Sigma-Aldrich), chloroform AR grade (without any further purification.

Synthesis of $Cs_4Cd_xMn_{1-x}Bi_2Cl_{12}$ nanocrystals (NCs):

The NCs were synthesized by hot-injection method.[30,31] 0.72 mmol of Cesium acetate, 0.36 mmol of bismuth acetate, 0.18 mmol of Cadmium acetate for x=1. (or 0.18 mmol of manganese acetate for x=0) were dissolved in 10ml of ODE, 2.5ml of OA and 0.7ml of OLAM in a 50ml 3-neck flask and heated to 110ºC under vacuum for 1hr (the color of the solution was pale yellow), after that the temperature was increased to 150ºC under an Argon atmosphere, then 2.16 mmol of TMSCl was injected (the color of the solution was turned into milky- white), after 1 min of injection the temperature of the synthesis was reduced to room temperature by ice bath. For purification the crude synthesis was centrifuged at 6000 rpm for 30min, then the supernatant was discard, the precipitate was dissolved in 5ml of Chloroform, depressed by vortex, then suspended with sonication for 5 min, later centrifuged again at 6000 rpm for 30min.

Again, the supernatant was discarded and the precipitate was dispersed in 5 ml chloroform and saved for measurements. Similar method was used to synthesize different ratios between Manganese and cadmium according to table 1S.

Characterizations:

Optical measurements: absorbance measurements were performed using a jasco V-670 spectrophotometer. Photoluminescence (Pl) measurements were performed by Horiba fluoromax-4 spectrofluorometer with 150W CW ozone free xenon arc lamp. The spectra were recorded using 360 nm excitation. Samples were diluted in chloroform then measured in quartz cuvettes

High-Resolution transmission electron microscopy (HRTEM): The morphology and the structure of the NCs were investigated using a Tecnai F20 microscope operated at 200kV.

Scanning TEM: high angle annular dark field scanning TEM (HAADF STEM) images for atomic resolution were picked up using a probe-corrected high resolution scanning transmission electron microscope, Z.

Elemental analysis EDS: energy dispersive X-ray spectroscopy was performed using Super-X EDS detector. For TEM and STEM analysis a thin copper grid coated with an ultrathin amorphous carbon was used.

Scanning tunneling spectroscopy (STS): The tunneling spectra were acquired using a home-built room-temperature STM and a Pt-Ir tip. The STM topographic images were

typically measured with sample-bias and current set values of V = 2-2.2 V (to be well above the CBM) and I = 0.5 nA, whereas the tunneling I-V curves were acquired with set values (before disabling the feedback loop for spectrum acquisition) of V = 1.8 V and I = 0.5 nA (in attempt to be as close as possible to the CBM and observe also in-gap states, but at the same time avoid apparent gap enhancement due to voltage distribution between the two tunnel junctions involved in the double-barrier configuration.[13,28] Our dI/dV-V tunneling spectra, which are proportional to the local density of states, were numerically derived from curves resulting by averaging over 5 I-V characteristics taken on each NP, in each of which the current was recorded, and averaged over, 64 times for every bias value.

References

[1] B. Vargas, E. Ramos, E. Pérez-Gutiérrez, J. C. Alonso and D. Solis-Ibarra, *J. Am. Chem. Soc.*, 2017, **139**, 9116–9119.

[2] Q. A. Akkerman and L. Manna, *ACS Energy Lett.*, 2020, 604–610.

[3] Y. Tang, L. Gomez, M. Van Der Laan, D. Timmerman, V. Sebastian, C. C. Huang, T. Gregorkiewicz and P. Schall, *J. Mater. Chem. C*, 2021, **9**, 158–163.

[4] P. Acharyya, K. Kundu and K. Biswas, *Nanoscale*, 2020, **12**, 21094–21117.

[5] J. Sun, J. Yang, J. I. Lee, J. H. Cho and M. S. Kang, *J. Phys. Chem. Lett.*, 2018, **9**, 1573–1583.

[6] F. H. Gourji and D. Velauthapillai, *Molecules*, 2021, **26**, 2010.

[7] H. Yang, T. Cai, E. Liu, K. Hills-Kimball, J. Gao and O. Chen, *Nano Res. 2019 131*, 2019, **13**, 282–291.

[8] R. S. Lamba, P. Basera, S. Bhattacharya and S. Sapra, *J. Phys. Chem. Lett.*, 2019, **10**, 5173–5181.

[9] S. Wu, W. Li, J. Hu and P. Gao, *J. Mater. Chem. C*, 2020, **8**, 13603–13611.

[10] B. Vargas, R. Torres-Cadena, D. T. Reyes-Castillo, J. Rodríguez-Hernández, M. Gembicky, E. Menéndez-Proupin and D. Solis-Ibarra, *Chem. Mater.*, 2020, **32**, 424–429.

11 S. E. Creutz, H. Liu, M. E. Kaiser, X. Li and D. R. Gamelin, *Chem. Mater.*, 2019, **31**, 4685–4697.

12 Y. Zhang, J. Yin, M. R. Parida, G. H. Ahmed, J. Pan, O. M. Bakr, J. L. Brédas and O. F. Mohammed, *J. Phys. Chem. Lett.*, 2017, **8**, 3173–3177

13 J. Li, J. Duan, X. Yang, Y. Duan, P. Yang and Q. Tang, *Nano Energy*, 2021, **80**, 105526.

14 Z. Deng, F. Wei, S. Sun, G. Kieslich, A. K. Cheetham and P. D. Bristowe, *J. Mater. Chem. A*, 2016, **4**, 12025–12029.

15 F. Zhang, Z. Ma, Z. Shi, X. Chen, D. Wu, X. Li and C. Shan, *Energy Mater. Adv.*, 2021, **2021**, 1–38.

16 T. Cai, W. Shi, S. Hwang, K. Kobbekaduwa, Y. Nagaoka, H. Yang, K. Hills-Kimball, H. Zhu, J. Wang, Z. Wang, Y. Liu, D. Su, J. Gao and O. Chen, *J. Am. Chem. Soc.*, 2020, **142**, 11927–11936.

17 S. Khalfin and Y. Bekenstein, *Nanoscale*, 2019, **11**, 8665–8679.

18 F. Igbari, Z. K. Wang and L. S. Liao, *Adv. Energy Mater.*, 2019, **9**, 1803150.

19 B. Yang, X. Mao, F. Hong, W. Meng, Y. Tang, X. Xia, S. Yang, W. Deng and K. Han, *J. Am. Chem. Soc.*, 2018, **140**, 17001–17006.

20 X. Li, X. Gao, X. Zhang, X. Shen, M. Lu, J. Wu, Z. Shi, V. L. Colvin, J. Hu, X. Bai, W. W. Yu and Y. Zhang, *Adv. Sci.*, 2021, **8**, 2003334.

21 B. Vargas, R. Torres-Cadena, J. Rodríguez-Hernández, M. Gembicky, H. Xie, J. Jiménez-Mier, Y. S. Liu, E. Menéndez-Proupin, K. R. Dunbar, N. Lopez, P. Olalde-Velasco and D. Solis-Ibarra, *Chem. Mater.*, 2018, **30**, 5315–5321.

22 N. P. Holzapfel, J. D. Majher, T. A. Strom, C. E. Moore and P. M. Woodward, *Chem. Mater.*, 2020, **32**, 3510–3516.

23 B. Vargas, D. T. Reyes-Castillo, E. Coutino-Gonzalez, C. Sánchez-Aké, C. Ramos, C. Falcony and D. Solis-Ibarra, *Chem. Mater.*, 2020, **32**, 9307–9315.

24 H. Yang, W. Shi, T. Cai, K. Hills-Kimball, Z. Liu, L. Dube and O. Chen, *Nanoscale*, 2020, **12**, 23191–23199

25 Y. P. Lin, S. Hu, B. Xia, K. Q. Fan, L. K. Gong, J. T. Kong, X. Y. Huang, Z. Xiao and K. Z. Du, *J. Phys. Chem. Lett.*, 2019, **10**, 5219–5225.

26 T. Cai, H. Yang, K. Hills-Kimball, J. P. Song, H. Zhu, E. Hofman, W. Zheng, B. M. Rubenstein and O. Chen, *J. Phys. Chem. Lett.*, 2018, **9**, 7079–7084.

27 U. Banin and O. Millo, *Annu. Rev. Phys. Chem.*, 2003, **54**, 465–492.

28 O. Ashkenazi, D. Azulay, I. Balberg, S. Kano, H. Sugimoto, M. Fujii and O. Millo, *Nanoscale*, 2017, **9**, 17884–17892.

29 A. Angi, R. Sinelnikov, A. Meldrum, J. G. C. Veinot, I. Balberg, D. Azulay, O. Millo and B. Rieger, *Nanoscale*, 2016, **8**, 7849–7853

30 N. Chen, T. Cai, W. Li, K. Hills-Kimball, H. Yang, M. Que, Y. Nagaoka, Z. Liu, D. Yang, A. Dong, C. Y. Xu, R. Zia and O. Chen, *ACS Appl. Mater. Interfaces*, 2019, **11**, 16855–16863.

31 F. Locardi, M. Cirignano, D. Baranov, Z. Dang, M. Prato, F. Drago, M. Ferretti, V. Pinchetti, M. Fanciulli, S. Brovelli, L. De Trizio and L. Manna, *J. Am. Chem. Soc.*, 2018, **140**, 12989–12995.